Landslides (2020) 17:2811-2824 DOI 10.1007/s10346-020-01451-1 Received: 26 September 2019 Accepted: 28 May 2020 Published online: 20 June 2020 © Springer-Verlag GmbH Germany part of Springer Nature 2020

Zhichen Song · Xiang Li · José J. Lizárraga · Lianheng Zhao · Giuseppe Buscarnera

Spatially distributed landslide triggering analyses accounting for coupled infiltration and volume change

Abstract Rainfall infiltration in unsaturated slopes alters the effective stress through pore water pressure changes, thus causing ground deformation. Although important to assess the timescale over which the margin of safety of a slope decreases, such coupled processes are rarely accounted in the context of spatially distributed hazard assessment procedures. In this paper, a physically based, spatially distributed model accounting for full hydro-mechanical coupling is discussed. The model relies on a vectorized finite element (FE) solver to calculate the stability of deformable unsaturated infinite slopes subjected to transient flow. First, the FE solver is used to study the response of individual slopes to a prolonged rainfall for three scenarios (i.e., rigid, swelling, and collapsible soil). Then, the model is used in the context of spatially distributed computations to assess spatiotemporal variations of factor of safety over a large area. For this purpose, a series of shallow landslides occurred in a mountainous landscape covered by collapsible loess deposits in northwestern China was used as test site. The analyses show that hydromechanical couplings affect the performance of the model in terms of computed failure time and areal extent of the unstable zones. Specifically, volume collapse due to suction decrease is found to reduce the time of failure compared with uncoupled computations obtained for a rigid soil scenario. The most substantial advantages of using coupled analyses have been reported with reference to gentle slopes, for which the higher rate of suction reduction driven by volume change was crucial to capture landslide source areas that would otherwise be overlooked by uncoupled analyses. The proposed methodology offers a complete tool for landslide hazard assessment, in that it incorporates sources of coupling between hydrology and mechanics that are crucial to replicate the physics of landslide initiation.

Keywords Hydro-mechanical coupling · Infiltration · Spatially distributed analysis · Unsaturated soils · Collapse

Introduction

Rainfall-induced landslides are among the most widespread and frequent hazards around the world (Petley 2012). Water infiltration is indeed a well-known source of soil strength deterioration, either by increasing pore water pressure (hence reducing the frictional resistance) or by changing the soil rheology through enhanced deformability and wetting-induced volume change (Alonso et al. 1990; Rahardjo and Fredlund 1995; Mihalache and Buscarnera 2016). Specifically, as water infiltrates in an unsaturated soil, suction and degree of saturation vary, eventually giving rise to alterations of the stresses acting on the skeleton and volume changes. At the same time, changes in the state of saturation controlled by the volume change response may affect the hydraulic characteristics of the soils, thus influencing the timescale of the infiltration process and the rate at which deformation and failure may occur (Wu and Zhang 2009; Garcia et al. 2011; Kim et al. 2016a, b). It is therefore apparent that, under the most general circumstances, water infiltration and soil are coupled, in that they affect each other and determine the hydro-mechanical response of natural unsaturated soil slopes (Zhang et al. 2005).

Several approaches have been used to evaluate rainfall-induced landslide hazards at regional scale, such as empirical rainfall threshold methods (Tiranti and Rabuffetti 2010; Godt et al. 2006; Brunetti et al. 2010; Salciarini et al. 2012; De Vita et al. 2013) or statistical and probabilistic methods based on historical records (Ohlmacher and Davis John 2003; Coe et al. 2004). Over the last decades, a growing number of physically based regional models for the assessment of rainfall-induced landslide susceptibility have also been proposed (Montgomery and Dietrich 1994; Iverson 2000; Salciarini et al. 2008; Baum et al. 2010; Lepore et al. 2012; Park et al. 2013; Su et al. 2015; Bui et al. 2017; Zhao et al. 2019). The recent improvement of the computing performance and the development of increasingly accessible geographical information system (GIS) platforms and remote-sensing technology have further contributed to the widespread use of such physically based models, by making them increasingly more powerful and reliable for regional-scale landslide forecasting. A crucial characteristic of such class of landslide assessment tools is the simulation of subsurface hydrologic processes in light of well-defined balance equations and constitutive relations. Although such models proved useful in several geological settings, they often recur to simplified descriptions of the soil behavior by neglecting the deformability prior to failure or hypothesizing frictional slip as the only mechanism originating instability. However, recent studies on the mechanics of shallow landslides have shown that volume changes prior to frictional failure play a crucial role for the triggering of shallow landslide in so-called collapsible soil, i.e., deposits which may experience volume loss upon water infiltration (Buscarnera and Prisco 2012; Buscarnera and Di Prisco 2013; Lizárraga et al. 2017). Such studies suggest that neglecting the coupling between water intake and soil rheology may lead to inaccurate assessments of the rate and magnitude of the deterioration of the margin of safety during a storm, thus potentially rendering the analysis unconservative.

The purpose of this paper is to take into account the coupling between fluid flow and deformation throughout the course of a rainstorm, thus acknowledging the role of volume changes on the transients that control the variation of pore pressure within a slope. In standard uncoupled models, a seepage analysis is used to predict pore water pressures within a given time, eventually using them as input in stability calculations (Cai and Ugai 2004; Yoo and Jung 2006). In such analyses, the soil is essentially assumed rigid, in that no soil property enters into the mass balance equations used to compute pore pressure transients. Abundant field and laboratory evidence, however, suggests that the hypothesis of rigid soil during infiltration may be overly restrictive. For example, Tabarsa et al. (2018) conducted a series of collapse potential tests on loess samples taken from a site susceptible to landslides, showing a significant risk for wetting-induced collapse. Along the same lines, Schulz et al. (2018) found a considerable role of swelling in the dynamics of slow-moving landslides in clay soils subjected to seasonal rainfall infiltration. In all these cases, it is arguable that the infiltration processes responsible for the strength deterioration that eventually led to ground failure took place within deformable soil slopes, thus being influenced by coupled fluid flow-deformation processes. The importance of hydro-mechanical couplings has been extensively documented in the context of individual slopes, for which the simultaneous solution of water mass and momentum balance equations leads to a better representation of the triggering process (Oh and Lu 2015; Yang et al. 2017; Hu et al. 2018; Soga et al. 2016). By contrast, no attempts have been made to explore the impact of hydro-mechanical couplings at the regional scale, where a more accurate description of pore pressure transients across a site may lead to substantial improvements of the landslide susceptibility computations (Lizárraga et al. 2017; Lizárraga and Buscarnera 2018).

For this purpose, in this paper a physically based model enabling for coupled hydro-mechanical computations is presented. The model relies on a vectorized finite element (FE) algorithm that combines stability analyses for infinite slopes with a transient, one-dimensional numerical solution of the hydrologic response of layers made of rigid, swelling, or collapsible soil. For this purpose, a brief description of the numerical model, as well as of the implementation procedures, is presented first. Afterwards, the model performance is illustrated with reference to individual slope units, with the purpose to elucidate differences between coupled and uncoupled scenarios. Finally, the model has been tested at the regional scale by using as a reference test site a series of shallow landslides that took place in northwestern China across a landscape covered by collapsible loess.

Model description

Equilibrium conditions

For an infinite slope as shown in Fig. 1, the balance of linear momentum for an incremental loading process is given by:

$$\frac{\partial \dot{\sigma}_z}{\partial z} + \dot{\gamma}_s \cos \alpha = 0, \quad \frac{\partial \dot{\tau}}{\partial z} - \dot{\gamma}_s \sin \alpha = 0$$
 (1)

where α is the slope angle, h the soil thickness, σ_z the total normal stress, τ the shear stress, z is the direction normal to the slope, γ_s the unit weight of the soil, and the upper dot denotes a time derivative. The constitutive relationships for the soil skeleton are hypothesized to be governed by the constitutive stress σ' (Sheng et al. 2003), which here will be used in a linear elastic context, as follows:

$$\sigma = \sigma' + \chi_k s \tag{2}$$

where s is the matric suction and χ_k is the coefficient that quantifies the effects of suction on the constitutive stress. This stress formulation is versatile enough to encompass both effective stress theories (e.g., Khalili and Khabbaz 1998; Lu and Likos 2006) and approaches based on dual independent variables (Rahardjo and Fredlund 1995; Alonso et al. 1990). For convenience, hereafter the latter approach will be followed, thus assuming $\chi_k = 0$. This choice gives flexibility to incorporate either swelling or collapse into the fluid flow equations by following the pseudo-elastic approach proposed by Lloret et al. (1987). At this reference, it must be noted that the stress expression in (2) can in principle be used also in other contexts, and may thus be used in future extensions of the methodology proposed here. An example is the case of constitutive

laws modeling volume collapse as a plastic phenomenon, either in the context of effective stress formulations or through double variable approaches (Buscarnera 2014).

Hydro-mechanical coupling governing equation

Based on water mass balance and Darcy's law, the governing equations for 1D hydro-mechanical coupling in unsaturated soils can be given by (Richards 1931):

$$n\frac{\partial S_r}{h}\dot{h} + S_rB\dot{\varepsilon} = K\nabla^2 h + \frac{\partial K}{\partial z} \times \cos\alpha \tag{3}$$

where h is the water pressure head, ε the normal strain, n the porosity, S_r the degree of saturation, B the Biot's coupling coefficient, and K the hydraulic conductivity.

The 1D stress-strain relationship associated with the normal strain can be expressed in incremental form as follows (Lloret et al. 1987):

$$\frac{\partial \varepsilon}{\partial t} = \frac{1}{E} \frac{\partial \sigma}{\partial t} + \frac{1}{F} \frac{\partial s}{\partial t} \tag{4}$$

where σ is the normal net stress, while E and F are the elastic moduli of the soil with respect to changes in the net stresses and soil suction, respectively. F is negative for collapsible soils, while is positive for swelling soils. Hereafter, the infiltration process is assumed to take place under fixed geometry and mechanical boundary conditions, thus implying constant total normal stress. As a result, changes in constitutive stress state within the unsaturated slope are uniquely related to pore water pressure (i.e., suction) variation. Under these hypotheses, Eq. (4) reduces to:

$$\frac{\partial \varepsilon}{\partial t} = \frac{1}{F} \frac{\partial s}{\partial t} \tag{5}$$

The mechanical constitutive relations are completed by the expression linking shear strain and stress, which in a linear elastic context is given by:

$$\frac{\partial \gamma}{\partial t} = \frac{1}{G} \frac{\partial \tau}{\partial t} \tag{6}$$

where G is the elastic shear modulus.

Based on Eq. (5), combining Eqs. (1) and (3), the system of coupled partial differential equations (PDEs) can be recast as

$$\frac{\partial}{\partial y} \left(E \dot{\varepsilon} \right) + \frac{\partial}{\partial y} \left(\frac{E}{F} \dot{s} \right) + \dot{\gamma}_{s} \cos \alpha = 0$$

$$\frac{\partial}{\partial y} \left(G \dot{\gamma} \right) - \dot{\gamma}_{s} \sin \alpha = 0$$
(7)

$$n\frac{\partial S_r}{h}\dot{h} + S_r B\frac{1}{F}\frac{\partial s}{\partial t} = K\nabla^2 h + \frac{\partial K}{\partial z} \times \cos\alpha$$

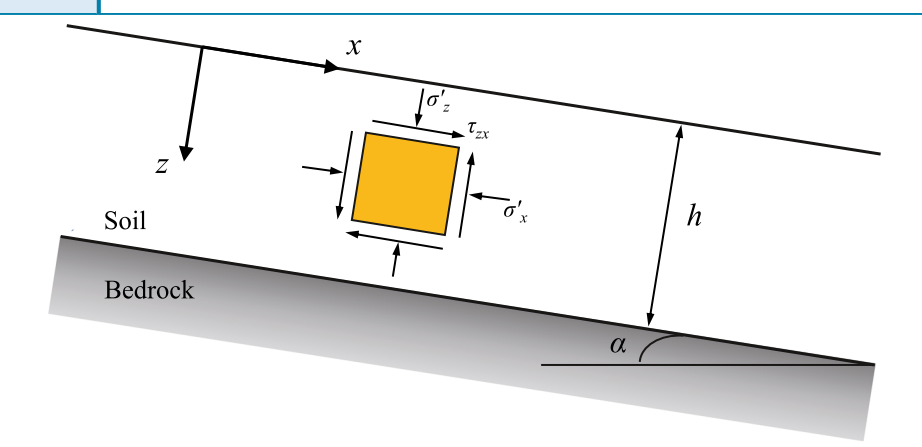


Fig. 1 A homogeneous infinite soil slope and its coordinate system

Additionally, suitable constitutive relations for the hydraulic variables have to be defined, by specifying a water retention curve (WRC) and a hydraulic conductivity function (HCF). Hereafter, the Gardner model is used for both the WRC and HCF, as follows:

$$\theta(h) = \theta_r + (\theta_s - \theta_r) \exp(-ah) \tag{8}$$

$$K(h) = K_s \exp(-ah) \tag{9}$$

where θ is the volumetric water content; θ_r and θ_s are the residual and saturated volumetric water content, respectively; K_s is the hydraulic conductivity at saturated condition; and ais a material constant that controls the suction sensitivity of both hydraulic conductivity and moisture content. Finally, the initial boundary-value problem (IBVP) can be solved by incorporating appropriate initial and boundary conditions.

Factor of safety

In order to assess stability conditions for an unsaturated slope, the factor of safety (FS) has to be defined. Although multiple FS expressions are in principle available, here the following expression valid for frictional failure will be used (Lizárraga et al. 2017):

$$FS = \frac{\tan \phi'}{\tan \alpha} \left(1 + \frac{ks}{\sigma^{net}} \right) \tag{10}$$

where ϕ' and α are friction angle of soil layer and slope angle, respectively; σ^{net} is the net stress and k is the parameter that quantifies the effect of suction on the shearing resistance. In other words, the following analyses postulate two independent contributions in the strength of unsaturated soils, namely frictional strength and suction. This approach is consistent with classical strength criteria for unsaturated soils and implies that the increase of shear stress at failure scales with suction increments through the constant coefficient $\tan \phi_b = k \tan \phi'$ (Fredlund et al. 1978).

Implementation

Performing spatially distributed analyses through the vectorization scheme proposed by Lizárraga and Buscarnera (2018) involves three stages, referred to as input, processing, and output. Here, this procedure has been further elaborated to solve coupled hydro-mechanical problems at each individual slope unit. Figure 2 illustrates the methodology. The first step involves a discretization procedure, by which features of the FE model such as mesh size and time steps are defined by taking into account the geometric attributes of the cells of the georeferenced grid (e.g., thickness). Then, the slopes of the landscape are arranged into j subsets sharing the same discretization parameters (marked as j =1 to 3 in Fig. 2 and denoted by different colors). The vectorized structure of the selected FE algorithm implies that the computations are performed simultaneously for all the slope units within a given subset j. Prior to the processing stage, meshing and time discretization is assigned to each classified subset (i) to guarantee reduced computational cost and accuracy.

During the second stage, the pore pressures and correspondent displacements are computed simultaneously. Next, the computed pore pressure is used to update FS for each cell in every time step. If at any time step, the condition $FS \le 1$ is met at certain depth throughout the analyzed slopes, the corresponding failure time and depth (tf and zf) are saved into output column vectors. Otherwise, the program keeps searching until the end of the storm (which is prescribed as the input loading), eventually assigning a non-data index to all the cells for which FS > 1 at all the stages of the analysis.

Finally, the computed output column vectors are mapped back to the original georeferenced grid by generating raster files for postprocessing and visualization which can be performed through a GIS platform.

Based on the abovementioned methodology, soils with different deformation characteristics can be simulated by switching the sign of the elastic modulus, F. This is important for slope stability analyses, in that coupled volume changes during infiltration may play an opposite role on the margin of safety reflected by the FS (Wu et al. 2016) or matric suction (Kim et al. 2016a, b). Therefore, to analyze the role of the hydro-mechanical couplings, three scenarios will be considered: (i) an uncoupled model (referred to as

Original Paper

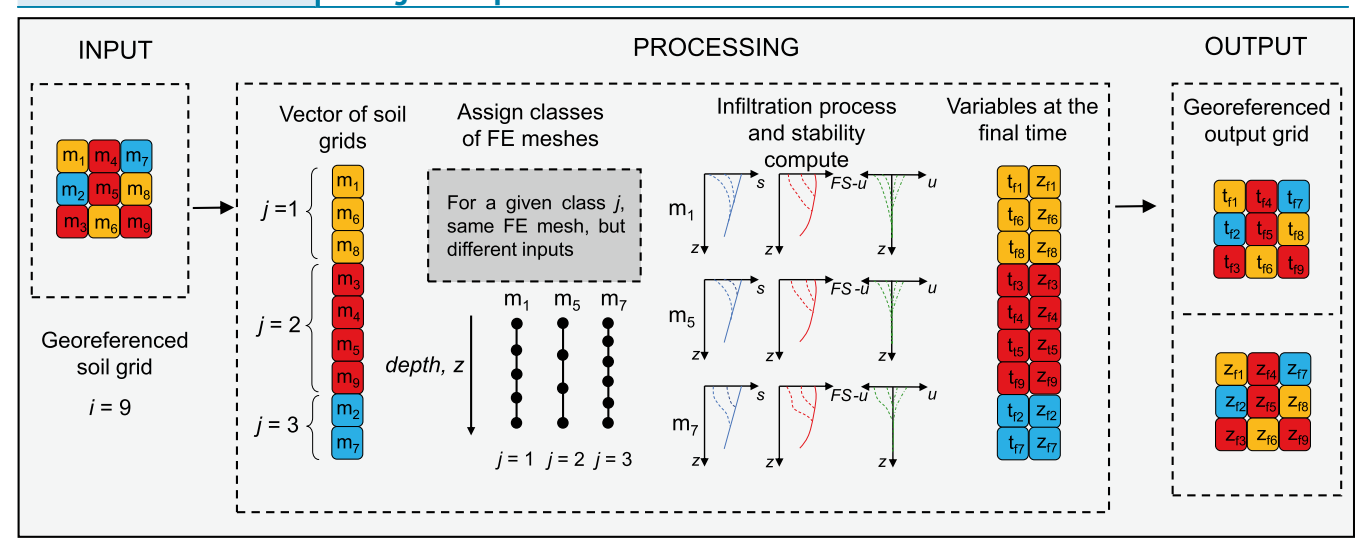


Fig. 2 Schematic representation of model workflow: m = number of cells, $j = number of cell classes with the same FE mesh, <math>t_f = failure time$, $z_f = failure depth$, s = failure time, $z_f = failure time$, $z_f = failure$ suction, FS = factor of safety, u_v = vertical displacement (modified from Lizárraga and Buscarnera 2018)

model A), which refers to the case of rigid soil (i.e., F in Eq. (4) is assumed infinitely large, such that suction changes do not imply volume change); (ii) a coupled model (referred to as model B) which refers to the case of swelling soil (F > 0); and (iii) a further coupled model (referred to as model C) which focuses on the case of collapsible soil (F < 0).

Single slope response

Before applying the proposed methodology to the selected study area, single slope analyses have been conducted. The simulations were based on free drainage conditions at the bottom of the slope and constant flux prescribed at its, thus enabling to verify our numerical computations against the analytical results recently obtained by Wu et al. (2016) with reference to analyses based on the same boundary conditions.

Figure 3 illustrates the variation of the water head during constant rain infiltration with reference to each of the three abovementioned model scenarios. The results of the model have been validated against the analytical solution proposed by Wu et al. (2016) for soils characterized by the same material properties used in the numerical analyses.

The results display perfect match between numerical and analytical results. Most notably, they show that the proposed numerical model is a convenient alternative to explore very general initial and boundary conditions typical of field settings. For a given rainfall intensity, higher suction loss corresponds to higher volume change, everything else being equal. This implies that more compliant soils will depart more substantially from the uncoupled scenario A (rigid soil). However, the type of volume change is also important. In particular, for the coupled model B (swelling soil) the computed pore water pressure changes are slower than those obtained with model A. In other words, swelling soils require longer time to experience a suction loss sufficient to cause an instability. By contrast, coupled model C (collapsible soil) displays faster suction loss than rigid soils (i.e., model A) and, consequently, enhanced tendency to achieve instability conditions.

With reference to the set of model parameters discussed earlier, two monitoring points from a single slope with inclination of 20° at the depth of 0.5 m and 2 m are selected to illustrate the computed evolution of key hydro-mechanical variables during infiltration.

Figure 4a shows the variation of suction for a constant rainfall input of 10⁻⁶ m/s. Compared with model A, scenario C exhibited a more pronounced suction loss at the depths of interest, while model B displayed a relatively slower suction decay. Such effects can be attributed to deformation-induced couplings. In fact, while

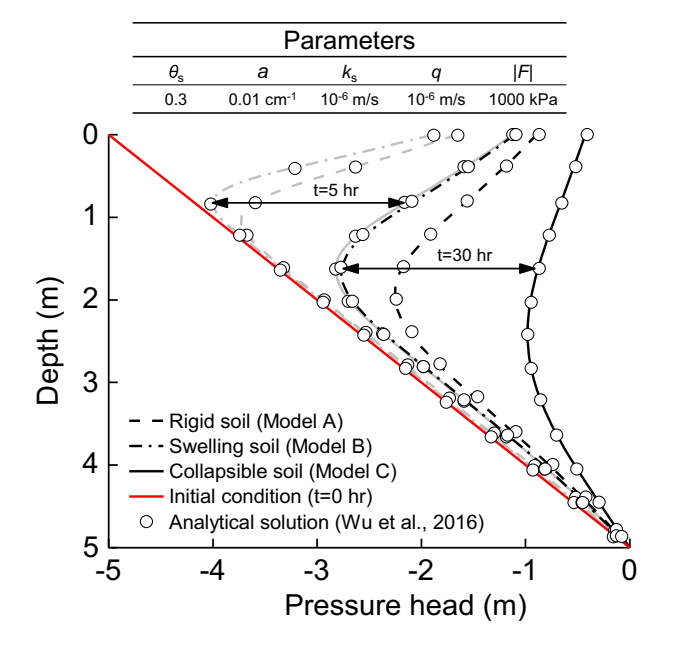


Fig. 3 Validation of the numerical model against analytical solutions reported by Wu et al. (2016). Scenarios relative to rigid, swelling, and collapsing soil are indicated by different line styles. Computations generated for constant rainfall $(q = 10^{-6} \text{ m/s})$ imposed during a time interval of 5 h (gray lines) and 30 h (black lines). Circles indicate the corresponding analytical solution

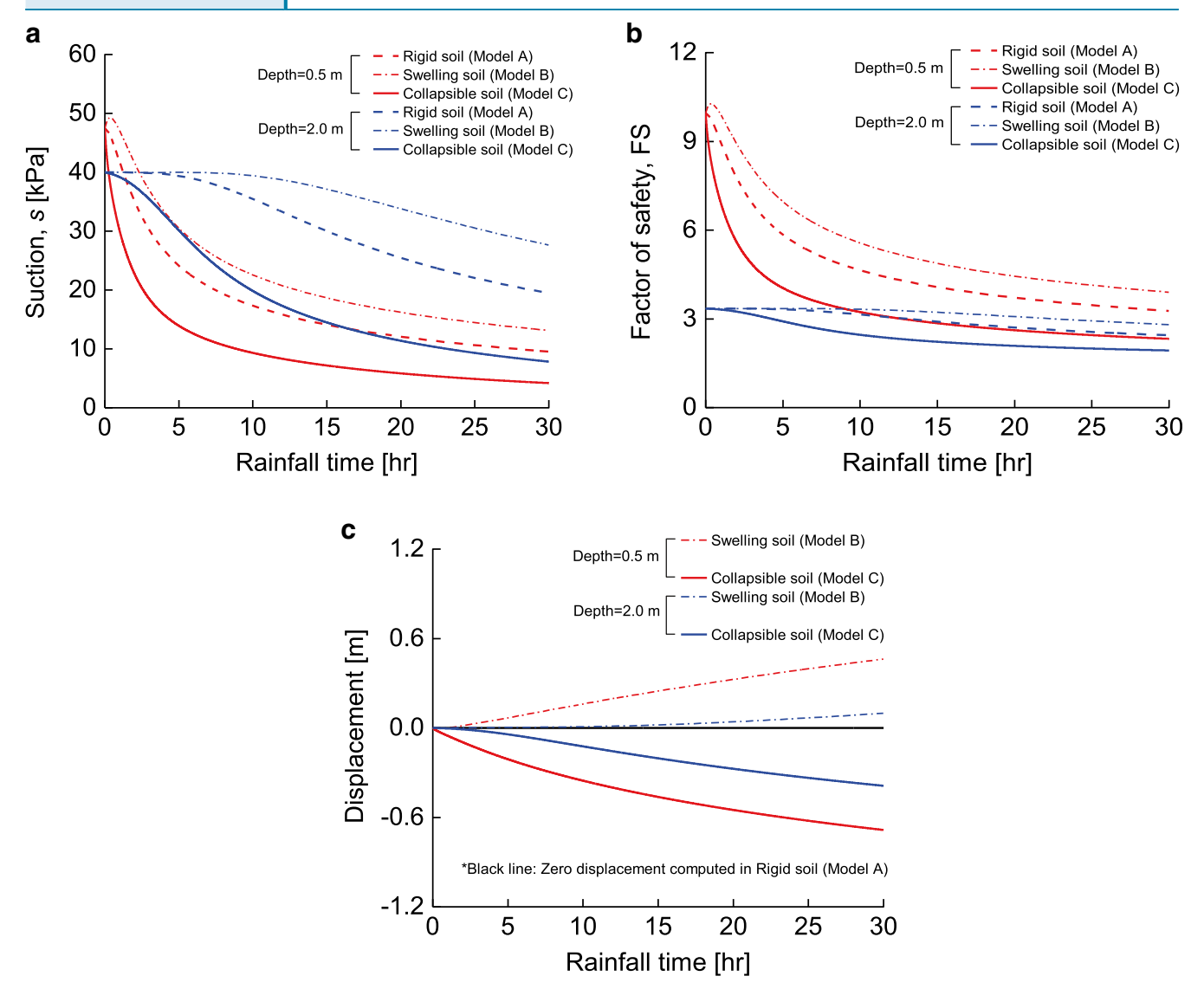


Fig. 4 Evolution of hydro-mechanical variables for different model scenarios; a suction; b FS; and c normal slope deformation

in model B such effect results from the relatively slow suction loss caused by swelling of the upper layers (which gives rise to a moderate suction increase beneath this zone to keep constant the rate of infiltration), in model C volume loss exacerbates suction decay, causing stronger downward infiltration even at deeper locations (depth = 2 m).

In addition, as the soil becomes more saturated, the coupling effects become less intense and the rate of suction loss follows similar trends. The sharp decrease of suction computed during this stage for all the model scenarios correspondingly resulted in a rapid decrease of FS (Fig. 4b). Although in all simulations, larger displacements are obtained in the upper portions of the slope due to higher levels of suction removal, Fig. 4c reveals distinct trends in soil deformation for the three models, characterized by negative displacements for model C (volume reduction due to collapse), positive displacements for model B (volume increase due to swelling), and no displacement during infiltration for model A (rigid soil). These predictions result from the use of a pseudo-elastic

constitutive law and can be enhanced by using elastoplastic constitutive laws incorporating a more general dependence of the soil compliance on mean confinement and shear stress (Gens et al. 2006).

Case study

This section discusses the features of a study area in the Xinjiang province, China, characterized by shallow landslide events that involved on loess deposits susceptible to volume change. Such study area will subsequently be used to test the proposed modeling methodology.

Characteristics of the site

The Yili Kazak autonomous prefecture, in the Xinjiang province, is one of the seventeen major geological disaster prevention and control areas listed by the Ministry of Land and Resource. Such classification is a consequence of the presence of a mountain belt

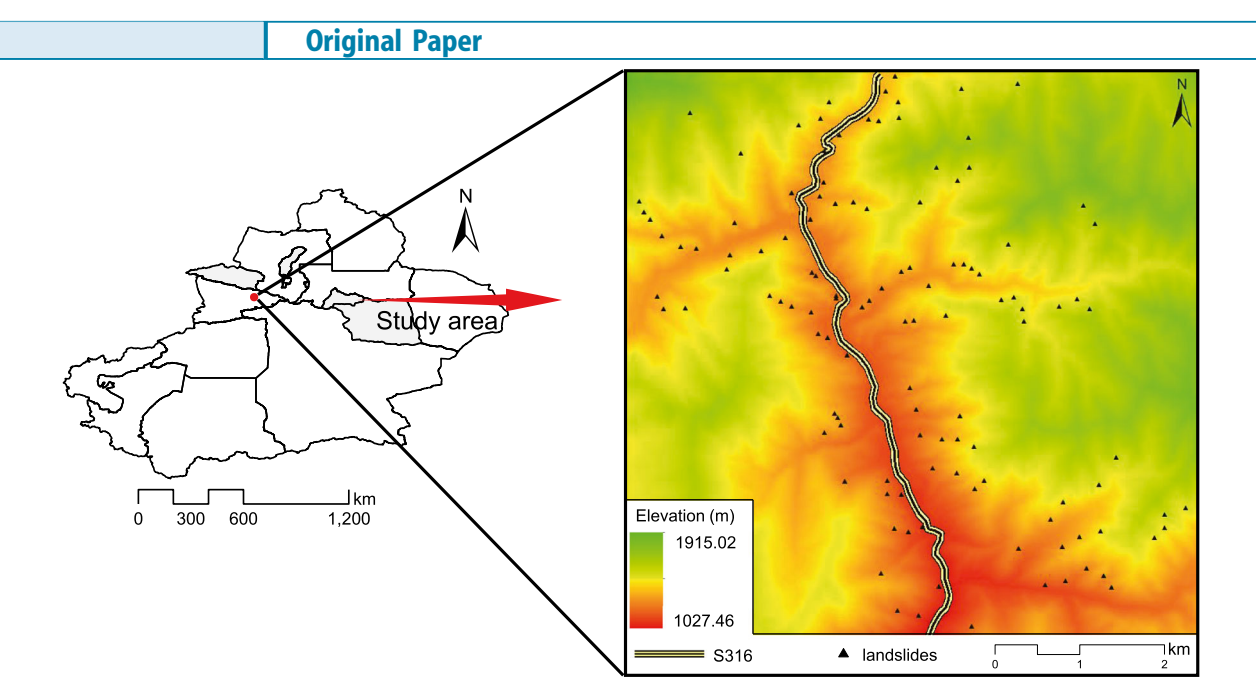


Fig. 5 Location of study area, landslide distribution, and digital elevation model (DEM)

covered by highly porous eolian deposits, which characterize the entire massif of the Yili Kazak region. The area is located alongside a provincial highway (S316) which connects the Nileke and Xinyuan county. Construction of highway S316, stretching more than 28 km, began in April of 2017. The main outcropping geological formations along the route are Quaternary Upper Pleistocene eolian deposits (Q3 eol), also called Malan loess, and Upper Pleistocene Holocene alluvial deposits (Q3-4pl) characterized by loose structure, coarse particles, and development of joint fissures. The annual precipitation amount is about 477 mm and most precipitation concentrated in April to July (Xinyuan County Meteorological Station). The high frequency of rainfall and the poor mechanical properties of the local soil caused continuous

landslides since the opening of the infrastructure, threatening traffic safety and nearby property.

On June 6-7, 2017, after more than 24 h of rainfall (including 12 h of heavy precipitation), dozens of shallow landslides were triggered across the massif covered by loess. The characteristics of the landslides were assessed by the local geological survey authorities through field investigations (GSR 2017), based on which the location of the landslide source areas was mapped across the region of interest (Fig. 5). Figure 6 illustrates examples of the typical landslides detected across the study area. According to the field investigation, most landslides failed at a depth lower than 5 m entirely within the Malan loess strata.

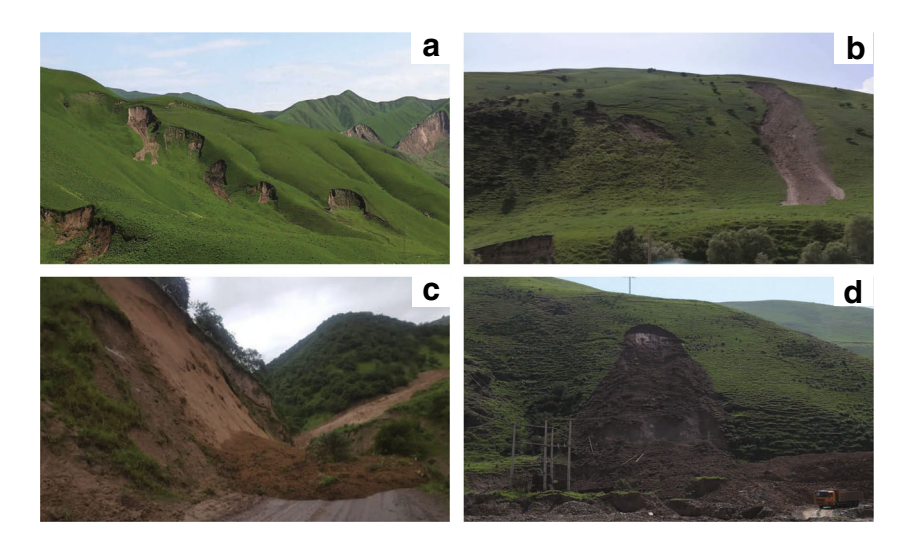


Fig. 6 Landslides triggered by heavy rainfall on June 6–7, 2017. The subfigures a-d illustrate examples of the detrimental impacts of landslides on the road safety (adapted from GSR 2017)

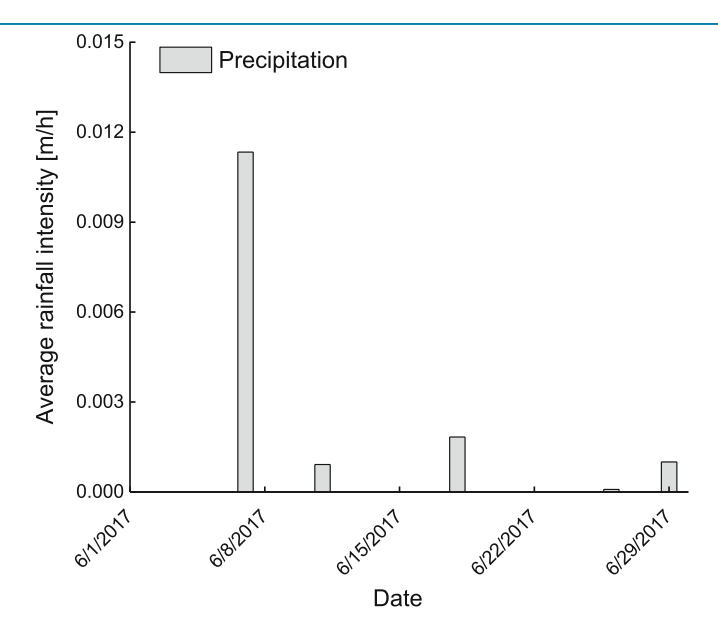


Fig. 7 Average daily precipitation intensity during June 2017 in Yili as reported by the China Meteorological Bureau

To simulate these events numerically, a georeferenced database has been created on the basis of these data, as well as of a digital elevation model (DEM) of 12 × 12 m resolution. In addition, rainfall intensity data from national meteorological stations are available for the study area. Figure 7 provides the average daily rainfall for the month of June 2017, showing that the event of June 7 was by far the most intense. The numerical analyses discussed in the following sections will therefore focus on this specific storm by using 12-h resolution rainfall measurements according to which the storm involved a first stage between 8:00 p.m. of June 6 and 8:00 a.m. of June 7, characterized by a relatively low average intensity of 0.0013 m/h (stage I) and a second stage from 8:00 a.m. to 8:00 p.m. of June 7, characterized by a higher average intensity of 0.0213 m/h (stage II), which triggered most of the reported landslides.

Hydrologic parameters

Initial hydrological conditions were measured on monitoring hillslopes within the area and reported in terms of degree of saturation (GSR 2017). Such monitoring data will be used here to calculate the initial suction conditions by using a WRC calibrated for Malan loess. The WRC calibration is shown in Fig. 8a, along with upper bound and lower bound retention characteristics derived from published experimental data (Li et al. 2018; Wu et al. 2011; Li et al. 2015; Wen and Yan 2014). Despite that the data scatter would suggest the need of sitespecific laboratory measurements here not available, an average calibration was used to provide a reasonable reference for the analyses. A calibrated HCF for Malan loess is shown in Fig. 8b, on the basis of the saturated value of K reported by Li et al. (2016). It can be seen that such calibration is in quantitative

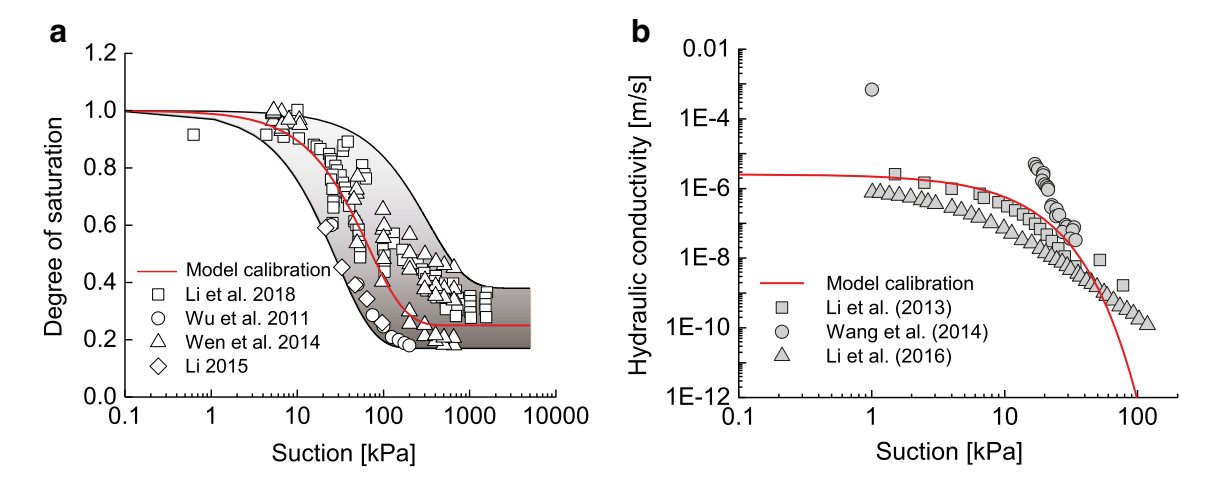
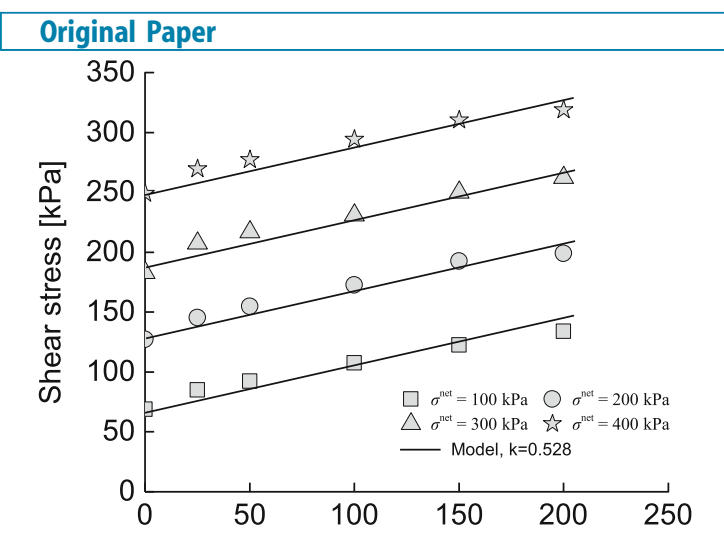


Fig. 8 Calibration of hydrologic parameters for the Malan loess. a Water retention curve (data after Li et al. 2018; Wu et al. 2011; Li et al. 2015; Wen and Yan 2014). b Hydraulic conductivity function (data after Li et al. 2013; Li et al. 2016; Wang et al. 2014). Parameter values corresponding to the Gardner model. Experimental data points are indicated by symbols. Solid lines indicate model results



Suction [kPa]

Fig. 9 Calibration of model parameters: coefficient controlling suction-induced strength increase (k = 0.528) (data after Hu et al. 2012)

agreement with data for other loess deposits from the area tested under unsaturated conditions (Li et al. 2013; Wang et al. 2014).

Mechanical parameters

The coefficient k in Eq. (10) controlling the suction dependence of the shearing resistance has been calibrated by fitting direct shear test data reported by Hu et al. (2012) (Fig. 9).

The parameter F is a modulus quantifying volume changes caused by suction variation (i.e., low values reflect high suction sensitivity and large deformation potential upon wetting). To estimate its value, oedometer test conducted on Malan loess under different vertical stress has been used (Shao et al. 2018) (Fig. 10). The results show pressure dependence of F, which exhibits higher magnitude in absolute value at higher pressure. This indicates more compliant response and high suction sensitivity near the surface. The value of F resulting from the experiments was negative for all the tested conditions, thus

indicating collapsible response. Accordingly, we can infer the modulus of F at low vertical stress, which led to an estimated value of 998 kPa for the simulations (the list of calibrated model parameters is summarized in Table 1). It must be noted that, as for all model parameters, direct evidence specific for samples taken from the study area would be ideal for quantitative analyses. Since this information was not available, the estimate derived from the data in Fig. 9 should be regarded only as a first approximation, which will be assessed against other model scenarios which will either neglect volume changes (model A) or assume the opposite type of volume change behavior (i.e., swelling, as in model B).

Analyses and results

Spatial performance

The computed susceptibility maps based on the calibrated parameters summarized in Table 1 are shown in Fig. 11. Cells with distinct

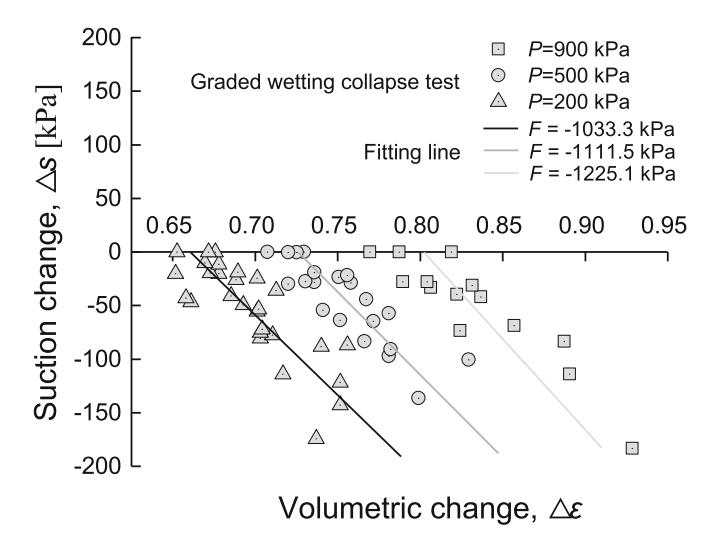
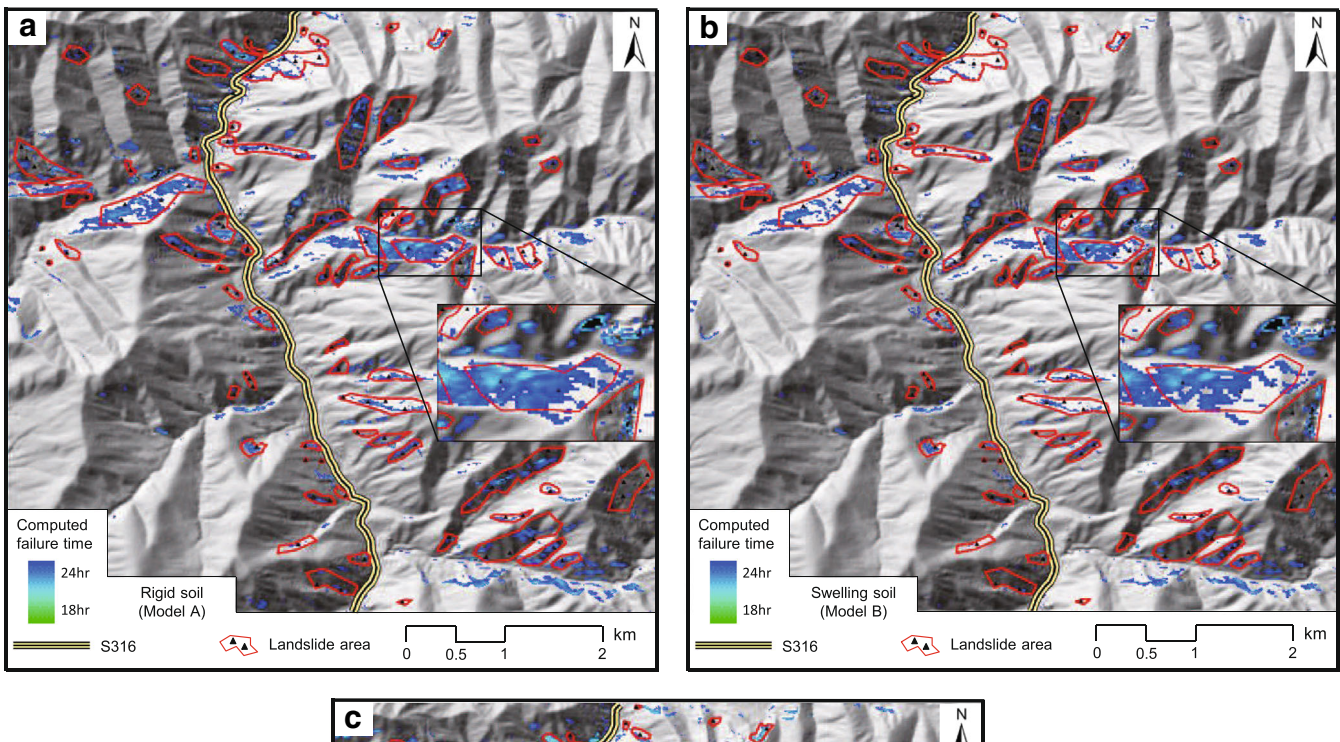


Fig. 10 Calibration of the elastic modulus F controlling suction-induced volume change (data after Shao et al. 2018); the best fit equation reported in the figure implies a value of F in kPa units

Table 1 Description of model parameters and calibrated values

Hydrologic parameters	Value	Mechanic parameters	Value
Saturated permeability, k_{sat} (m/s)	2.6E-6	Friction angle, ϕ' (°)	33
Residual volumetric water content, θ_{res}	0.115	Elastic moduli, E (kPa)	46,000
Gardner model, α (m ⁻¹)	0.15	Elastic moduli, $ F $ (kPa)	998
Unit weight of water, $\gamma_{\rm w}$ (kN/m³)	10	Unit weight of soil, $\gamma_{ m s}$ (kN/m 3)	15.6
Porosity	0.46	Suction sensitivity of shear strength, \boldsymbol{k}	0.528



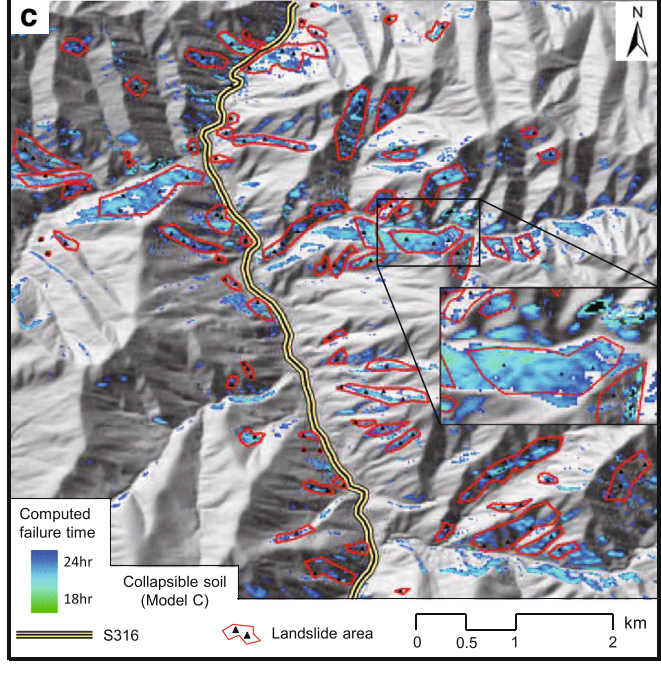


Fig. 11 Results of simulations for three model scenarios. a Uncoupled model A. b Coupled model B, swelling soil. c Coupled model C, collapsible soil

Original Paper QUANTITATIVE INDEXES: Study area number of reported triggering areas Reported triggering area number of computed unstable area within the triggering area Computed unstable area within the triggering area number of computed unstable Computed unstable area outside area outside the triggering area the triggering area

Fig. 12 Schematic diagram of the performance indices definition

colors indicate slope failure at different times, thus readily providing a visual snapshot of the spatial model performances. In addition, selected locations of the simulated area have been enlarged to facilitate the visualization of the temporal performance of the tested models. The map refers to the uncoupled model A (Fig. 11a), as well as to the coupled models B (Fig. 11b) and C (Fig. 11c). It is apparent that model C exhibits the highest density of failure zones across the landscape, while coupled model B predicted the lowest fraction of unstable areas. By contrast, the uncoupled model A produced intermediate predictions between the two coupled models. This result is in agreement with earlier analyses for individual slopes, which showed that volume collapse was

detrimental for slope stability, while swelling caused delayed suction removal.

To quantify the accuracy of the computations, two indicators here defined Success Index (SI) and Error Index (EI) are used to evaluate the model performance (Sorbino et al. 2007). Figure 12 schematically illustrates the definition of such indices. Specifically, SI represents the portion of computed unstable area that lies within each source area, while EI represents the percentage ratio of unstable predictions that lies outside the reported source area (Aout) and the area unaffected by the storm (Astable). Since high values of SI are generally accompanied by overprediction, the ratio SI/EI is used to assess the overall quality of the computation. For

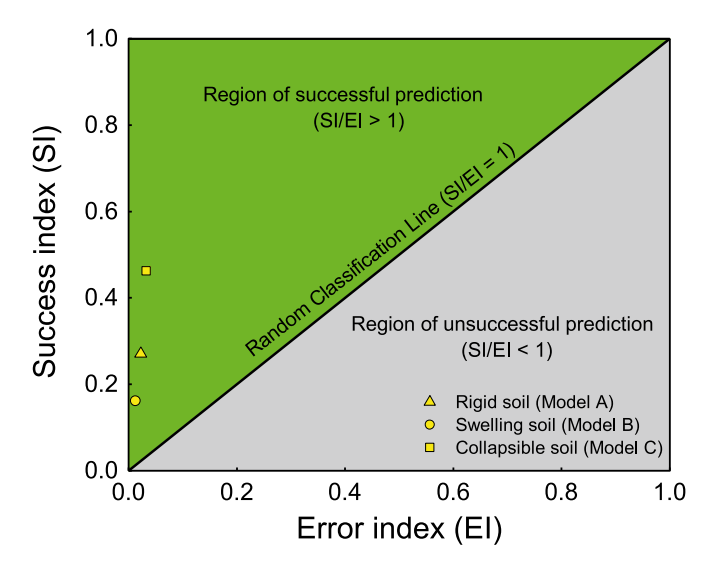


Fig. 13 Spatial performance of different model scenarios evaluated through the Success Index (SI) and the Error Index (EI). The light gray area indicates successful predictions (SI/EI > 1), while the dark gray area indicates poor predictions (SI/EI < 1)

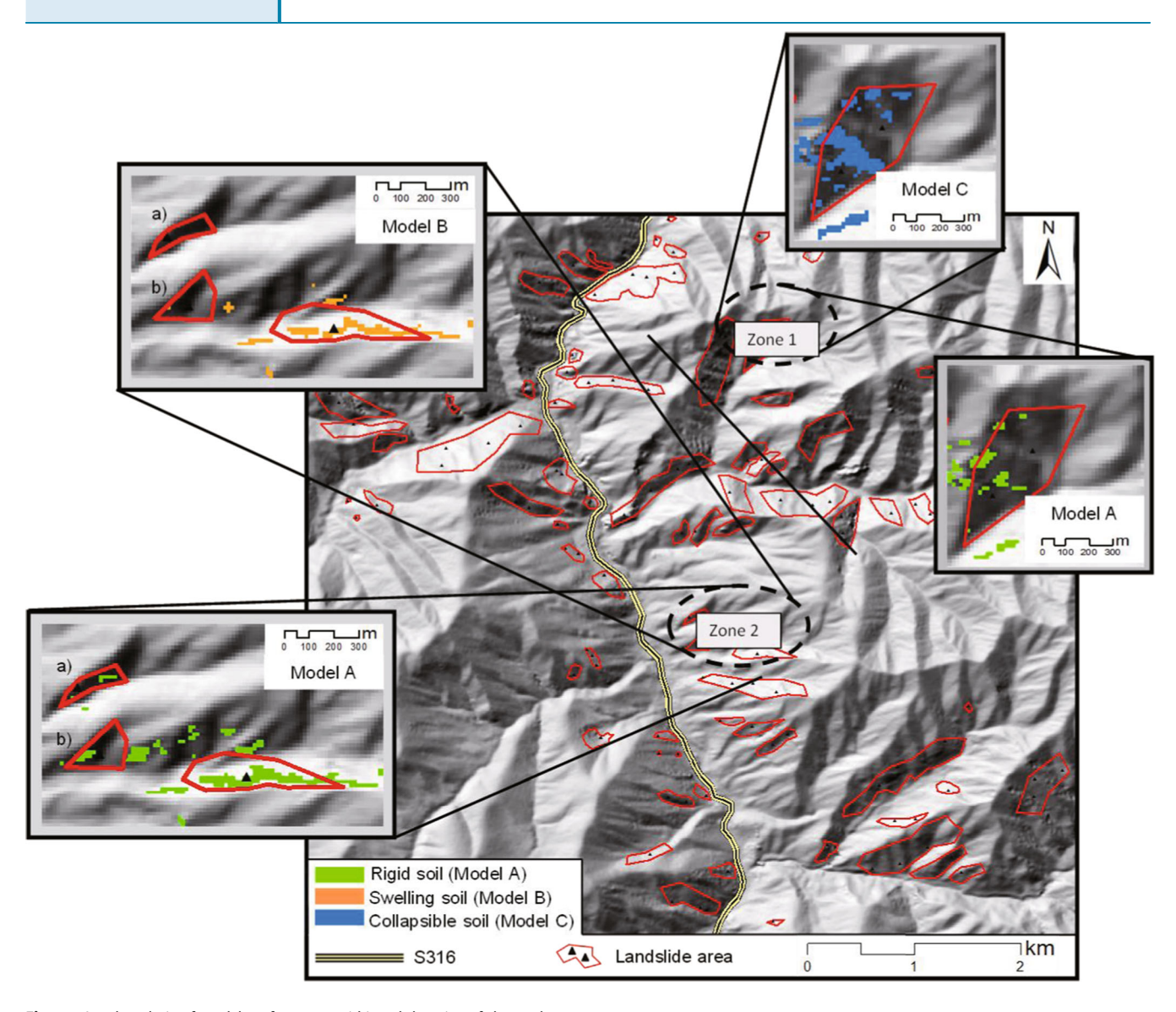


Fig. 14 Local analysis of model performance within subdomains of the study area

example, the so-called random classification line (RCL) refers to SI/EI = 1, a situation that describes the transition from an acceptable model characterized by SI/EI > 1 to a poor model characterized by an excess of error (Kim et al. 2016a, b).

Figure 13 illustrates the model performance by quantifying SI and EI for different scenarios. Each simulated case corresponds to a point and the ratio SI/EI can be used to assess the relation between correct predictions and overpredictions. It is readily apparent that model C is characterized by the highest percentage of successful slope failure predictions, with an SI of 46%. By contrast, model B and model A are characterized by SI 27% and 19%, respectively. A higher value of SI, however, usually comes at the expense of increasing values of EI. Also, in this case, model C is characterized by the largest level of overprediction (EI = 3.3%), compared with lower values of EI for both model A (EI = 2.3%) and B (EI = 1.4%). Despite these differences, model C can be shown to be the scenario characterized by the most favorable ratio

Table 2 Quantitative indexes comparison in two subdomains under different scenarios

Model	Zone 1 SI (%)	EI (%)	SI/EI	Zone 2 SI (%)	EI (%)	SI/EI
Rigid soil (model A)	6.92	1.97	3.51	24.17	2.23	10.82
Swelling soil (model B)	-	-	-	15	1.06	14.18
Collapsible soil (model C)	23.7	3.37	7.03	-	-	-

Original Paper

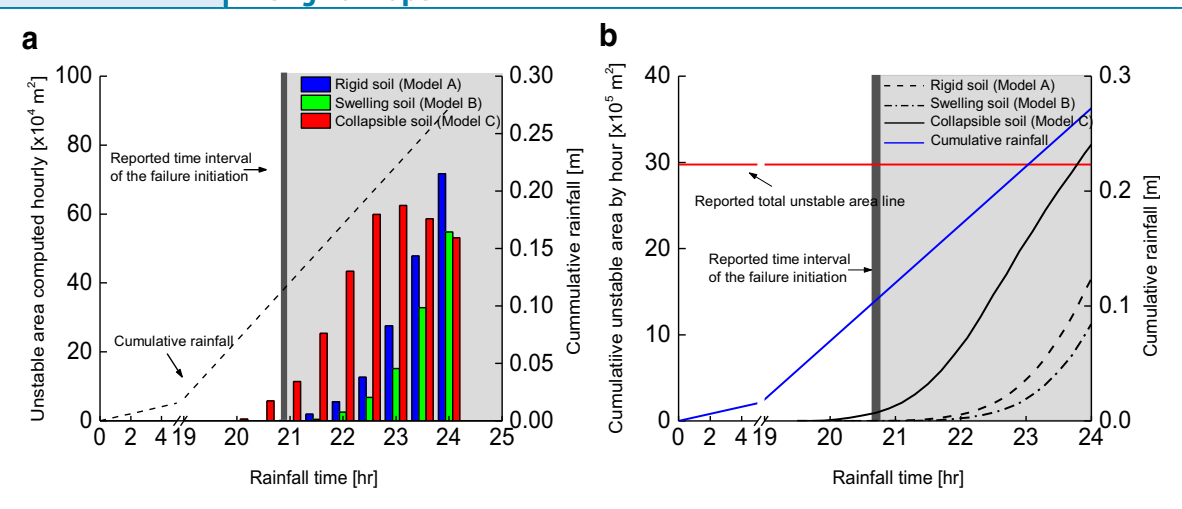


Fig. 15 Evolution of unstable areas across the study site. a Hourly rates of mobilized unstable areas computed by the three selected model scenarios. b Temporal evolution of the cumulative unstable area for the entire landscape

between correct predictions and false positives, in that it produces the highest SI/EI ratio (SI/EI = 14.1, compared with SI/EI = 11.9 and 12.7 of model A and B, respectively). At this reference, it is worth noting that, although model B produced the lowest amount of successful predictions, it also led to a relatively smaller degree of overprediction compared with the uncoupled scenario simulated through model A.

To further illustrate how coupling affects the results in terms of local SI and EI, two subdomains marked as zone 1 and 2 were chosen in Fig. 14. From zone 1, it can be seen that coupled model C provides more accurate predictions than the uncoupled scenario by obtaining SI = 23.7%, which is more than three times higher than that the result obtained with model A (SI = 6.92%). This benefit comes at a relatively limited cost in terms of overprediction, considering that model C and A in the same region resulted into SI/EI = 7.03 and 3.51, respectively. Similarly, zone 2 can be used to compare the predictions of coupled model B and model A. In fact, although the former predicts no failure within polygons a) and b), it also results in less overprediction throughout the selected zone than uncoupled model A (see results in Table 2 for a quantitative comparison).

These results indicate that for this particular case study, an uncoupled model (A) leads to relatively lower prediction accuracy, while coupled models may either offer more successful predictions (model C) or may limit the degree of overprediction (model B).

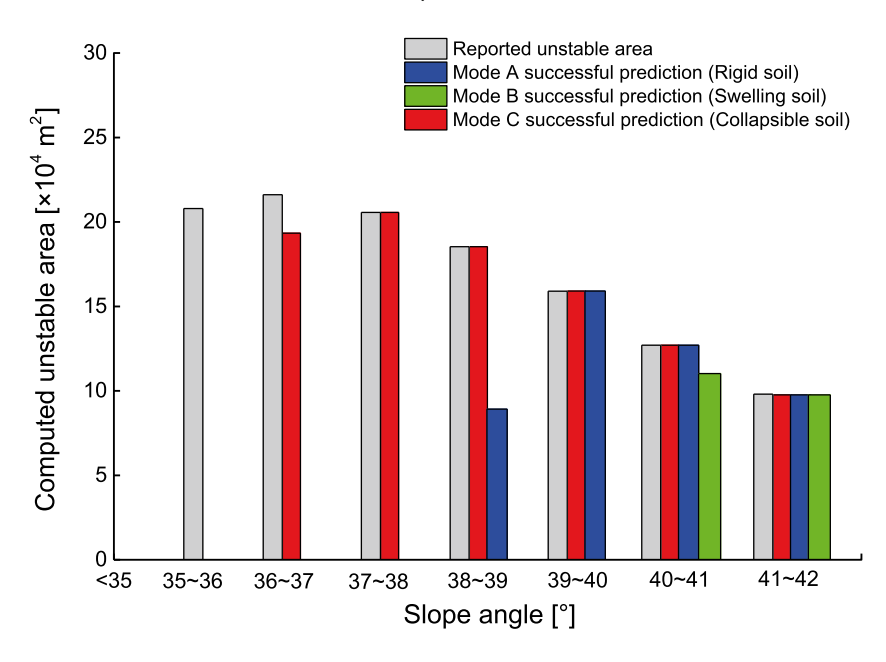


Fig. 16 Comparison of the performance of the three selected model scenarios in terms of computed unstable areas for different classes of slope angle. Model A indicates rigid soil (uncoupled scenario), model B indicates swelling soil (coupled analysis), and model C indicates collapsible soil (coupled analysis)

Temporal performance

Since physically based models based on different assumptions may lead to similar spatial patterns of ground failure within some subdomains of the study area, further insight on the advantages and disadvantages of each model scenario may be obtained by inspecting the computed temporal response (Lizárraga and Buscarnera 2018). Although such step is constrained by the scarcity of data for the considered event, limited information about the initiation time indicate that landsliding started after nearly 21 h from the start of the event (GSR 2017).

Figure 15a reports the hourly unstable area computed by the three model scenarios, while Fig. 15b shows instead the temporal evolution of the computed unstable area. It can also be noted that model A and B are characterized by a monotonic growth of the rate of failures during the storm, while model C is characterized by a peak of landslide intensity more than 0.6 km 2 at t = 23 h. In addition, the results indicate that for the scenario characterized by a collapsible soil (model C), the first unstable cells were computed after slightly less than 20 h of rainfall (t = 19.85 h), while for model A (non-deformable soil) and model B (swelling soil), the first unstable cells were computed at t = 21 h and t = 121.4 h. It can therefore be concluded that, although all models provide an estimate that is very close to the actual reported initiation time, model C provides the most conservative assessment of the onset of landslide, as well as the clearest identification of the time of peak landslide activity (i.e., t = 23 h).

Coupling sensitivity

Figure 16 illustrates the model performance by differentiating it in terms of slope angle of the cells across the study site. It is readily apparent that all models predict accurately failure within slope angle steeper than 41°, thus being in good agreement with documented field surveys. However, different models provide considerably different performance at more moderate slope inclinations (less than 41°), suggesting that accurate consideration of coupling effects is crucial for relatively gentle slopes, for which pre-failure deformations involving volume change have longer time to develop prior to frictional slip. Such results may be important in the analysis of highly mobile landslides, which are more likely to occur in gentle slopes susceptible to full saturation and liquefaction instabilities (Take and Beddoe 2014; Buscarnera and Prisco 2012; Buscarnera and Di Prisco 2013).

Conclusions

This work has assessed the influence of hydro-mechanical coupling on regional-scale landslide susceptibility. A physically based model with full hydro-mechanical coupling has been presented. The model allows the prediction of the spatiotemporal distribution of slope failures across a site by simulating the interplay between hydrological processes and soil deformation, as well as by computing the deterioration of the factor of safety associated with the resulting pore pressure transients by means of infinite slope stability analyses.

The model was used to analyze a series of landslides that occurred in northwestern China in June 2017 across a site covered by weak, suctionsensitive loess deposits. The model parameters have been constrained on the basis of field and laboratory evidence from the region, thus generating three distinct model scenarios for the computation of pore pressure transient (an uncoupled model reflecting rigid soil and two coupled models reflecting swelling and collapsing soil behavior). The results of single slope analyses indicate that coupling effects on

unsaturated slopes subjected to infiltration differed considerably, in that soil compaction upon wetting exacerbated the potential for instability while swelling led to slower suction loss and delayed ground failure. Such feedbacks were also found to affect the computed spatial-temporal patterns of shallow landslides in the selected case study. Although all models provided predictions consistent with the available field evidences, the coupled models led to a better spatial performance with higher ratio of SI/EI compared with the uncoupled model scenario. At the same time, despite the lack of information about the exact time of failure resulting from the considered rainstorm event, model C resulted in the most conservative estimate of the landslide initiation time compared with other models. Such results suggest that neglecting the role of flow-deformation couplings in landslide stability analyses may lead to losses in model accuracy, as well as unconservative results. This latter aspect was further emphasized by the inspection of the model performance for different classes of slope inclinations. It was found that hydro-mechanical coupling has negligible impact on steep slopes, while it is crucial to capture initiation mechanisms in more gentle slopes. Such result indicates that couplings cannot be neglected in landslide types taking place at stress conditions far from the threshold of frictional failure, and which therefore require further feedbacks to initiate an instability (e.g., loose structure prone to develop excess pore pressure, volume collapse, and liquefaction).

Acknowledgments

The first author acknowledges Professor Tonglu Li who provided case study data. The authors are also grateful to DLR for the TanDEM-X datasets distributed through proposal DEM-GEOL2292.

Funding information

This study was supported by the US National Science Foundation through grant ICER-1854951. Support of the Fundamental Research Funds for the Central Universities of Central South University (2018zzts032) is also gratefully acknowledged. The study was also financially supported by the China Scholarship Council (CSC).

References

Alonso EE, Gens A, Josa A (1990) A constitutive model for partially saturated soils. Géotechnique 40(3):405-430

Baum RL, Godt JW, Savage WZ (2010) Estimating the timing and location of shallow rainfall-induced landslides using a model for transient, unsaturated infiltration. J Geophys Res Earth Surf 115(F3)

Brunetti MT, Peruccacci S, Rossi M, Luciani S, Valigi D, Guzzetti F (2010) Rainfall thresholds for the possible occurrence of landslides in Italy. Nat Hazard Earth Sys 10(3):447-458

Bui DT, Tuan TA, Hoang ND, Thanh NQ, Nguyen DB, Van Liem N, Pradhan B (2017) Spatial prediction of rainfall-induced landslides for the Lao Cai area (Vietnam) using a hybrid intelligent approach of least squares support vector machines inference model and artificial bee colony optimization. Landslides 14(2):447-458

Buscarnera G (2014) Uniqueness and existence in plasticity models for unsaturated soils. Acta Geotech 9(2):313-327

Buscarnera G, Di Prisco C (2013) Soil stability and flow slides in unsaturated shallow slopes: can saturation events trigger liquefaction processes. Géotechnique 63(10):801-817

Buscarnera G, Prisco CD (2012) Discussing the definition of the second-order work for unsaturated soils. Int J Numer Anal Met 36(1):36-49

Original Paper

- Cai F, Ugai K (2004) Numerical analysis of rainfall effects on slope stability. Int J Geomech 4(2):69-78
- Coe JA, Michael JA, Crovelli RA, Savage WZ (2004) Probabilistic assessment of precipitation-triggered landslides using historical records of landslide occurrence, Seattle, Washington. Environ Eng Geosci 10:103-122
- De Vita P, Napolitano E, Godt JW, Baum RL (2013) Deterministic estimation of hydrological thresholds for shallow landslide initiation and slope stability models: case study from the Somma-Vesuvius area of southern Italy. Landslides 10(6):713-728
- Fredlund D, Morgenstern NR, Widger R (1978) The shear strength of unsaturated soils. Can Geotech J 15(3):313-321
- Garcia E, Oka F, Kimoto S (2011) Numerical analysis of a one-dimensional infiltration problem in unsaturated soil by a seepage-deformation coupled method. Int J Numer Anal Met 35:544-568
- Gens A, Sánchez M, Sheng D (2006) On constitutive modelling of unsaturated soils. Acta Geotech 1(3):137-147
- Godt JW, Baum RL, Chleborad AF (2006) Rainfall characteristics for shallow landsliding in Seattle, Washington, USA. Earth Surf Process Landf 31(1):97-110
- GSR (Geological Survey Report) (2017) Landslides survey reports on S316, 28th June 2017, Xinjiang transportation planning investigation design and Research Institute
- Hu T, Shao SJ, Li XL, Ma XT (2012) Experimental study of the characteristic parameters and structural behavior of loess. Chn Civ Eng J 7:148-154
- Hu R, Hong JM, Chen YF, Zhou CB (2018) Hydraulic hysteresis effects on the coupled flow-deformation processes in unsaturated soils: numerical formulation and slope stability analysis. Appl Math Model 54:221-245
- Iverson RM (2000) Landslide triggering by rain infiltration. Water Resour Res 36(7):1897-1910
- Khalili N, Khabbaz MH (1998) A unique relationship of chi for the determination of the shear strength of unsaturated soils. Géotechnique 48(5):681-687
- Kim Y, Jeong S, Kim J (2016a) Coupled infiltration model of unsaturated porous media for steady rainfall. Soils Found 56(6):1071-1081
- Kim MS, Onda Y, Uchida T, Kim JK (2016b) Effects of soil depth and subsurface flow along the subsurface topography on shallow landslide predictions at the site of a small granitic hillslope. Geomorphology 271:40-54
- Lepore C, Kamal SA, Shanahan P, Bras RL (2012) Rainfall-induced landslide susceptibility zonation of Puerto Rico. Environ Earth Sci 66(6):1667-1681
- Li P, Li TL, Wang H, Liang Y (2013) Soil-water characteristic curve and permeability prediction on Childs & Collis-Geroge model of unsaturated loess. Rock Soil Mech \$2:184-189
- Li P, Zhang X, Shi H (2015) Investigation for the initiation of a loess landslide based on the unsaturated permeability and strength theory. Geoenviron Disasters 2(1):24
- Li P, Li TL, Vanapalli SK (2016) Influence of environmental factors on the wetting front depth: a case study in the Loess Plateau. Eng Geol 214:1-10
- Li P, Li TL, Vanapalli SK (2018) Prediction of soil-water characteristic curve for Malan loess in Loess Plateau of China. J Central South Uni 25(2):432-447
- Lizárraga JJ, Buscarnera G (2018) Spatially distributed modeling of rainfall-induced landslides in shallow layered slopes. Landslides, 1-11
- Lizárraga JJ, Frattini P, Crosta GB, Buscarnera G (2017) Regional-scale modelling of shallow landslides with different initiation mechanisms: sliding versus liquefaction. Eng Geol 228:346-356
- Lloret A, Gens A, Batlle F, Alonso EE (1987) Flow and deformation analysis of partially saturated soils. Proc., 9th Eur. Conf. Soil Mech. Found. Eng., A. A. Balkema, ed., Dublin, 2, 565-568
- Lu N, Likos WJ (2006) Suction stress characteristic curve for unsaturated soil. J Geotech Geoenviron 132(2):131-142
- Mihalache C, Buscarnera G (2016) Controllability criteria for soils saturated by a compressible fluid. J Eng Mech 142(10):04016076
- Montgomery DR, Dietrich WE (1994) A physically based model for the topographic control on shallow landsliding. Water Resour Res 30(4):1153-1171
- Oh S, Lu N (2015) Slope stability analysis under unsaturated conditions: case studies of rainfall-induced failure of cut slopes. Eng Geol 184:96-103
- Ohlmacher GC, Davis John C (2003) Using multiple logistic regression and GIS technology to predict landslide hazard in northeast Kansas, USA. Eng Geol 69(3):331-343
- Park HJ, Lee JH, Woo I (2013) Assessment of rainfall-induced shallow landslide susceptibility using a GIS-based probabilistic approach. Eng Geol 161:1-15
- Petley D (2012) Global patterns of loss of life from landslides. Geology 40:927-930 Rahardjo H, Fredlund DG (1995) Experimental verification of the theory of consolidation
- for unsaturated soils. Can Geotech J 32(5):749-766 Richards LA (1931) Capillary conduction of liquids through porous mediums. Physics 1(5):318-333

- Salciarini D, Godt JW, Savage WZ, Baum RL, Conversini P (2008) Modeling landslide recurrence in Seattle, Washington, USA. Eng Geol 102(3-4):227-237
- Salciarini D, Tamagnini C, Conversini P, Rapinesi S (2012) Spatially distributed rainfall thresholds for the initiation of shallow landslides. Nat Hazards 61(1):229-245
- Schulz WH, Smith JB, Wang G, Jiang Y, Roering JJ (2018) Clayey landslide initiation and acceleration strongly modulated by soil swelling. Geophys Res Lett 45(4):1888-1896
- Shao X, Zhang H, Tan Y (2018) Collapse behavior and microstructural alteration of remolded loess under graded wetting tests. Eng Geol 233:11-22
- Sheng D, Sloan SW, Gens A, Smith DW (2003) Finite element formulation and algorithms for unsaturated soils. Part I: theory. Int J Numer Anal Methods Geomech 27(9):745-
- Soga K, Alonso E, Yerro A, Kumar K, Bandara S (2016) Trends in large-deformation analysis of landslide mass movements with particular emphasis on the material point method. Géotechnique 66(3):248-273
- Sorbino G, Sica C, Cascini L, Cuomo S (2007) On the forecasting of flowslides triggering areas using physically based models. In Proceedings of 1st North American landslides conference (Vol. 1, pp. 305-315). AEG Special Publication
- Su C, Wang L, Wang X, Huang Z, Zhang X (2015) Mapping of rainfall-induced landslide susceptibility in Wencheng, China, using support vector machine. Nat Hazards 76(3):1759-1779
- Tabarsa A, Latifi N, Meehan CL, Manahiloh KN (2018) Laboratory investigation and field evaluation of loess improvement using nanoclay-a sustainable material for construction. Constr Build Mater 158:454-463
- Take WA, Beddoe RA (2014) Base liquefaction: a mechanism for shear-induced failure of loose granular slopes. Can Geotech J 51(5):496-507
- Tiranti D, Rabuffetti D (2010) Estimation of rainfall thresholds triggering shallow landslides for an operational warning system implementation. Landslides 7(4):471-
- Wang H, Li TL, Fu YK (2014) Determination of permeability curve of unsaturated loess by transient profile method. J Hydraul Eng 45(8):997-1003
- Wen BP, Yan YJ (2014) Influence of structure on shear characteristics of the unsaturated loess in Lanzhou, China. Eng Geol 168:46-58
- Wu LZ, Zhang LM (2009) Analytical solution to 1d coupled water infiltration and deformation in unsaturated soils. Int J Numer Anal Met 33:773-790
- Wu YL, Xiang W, Zhao D (2011) Research on soil-water characteristic curve of unsaturated Malan loess. Saf Environ Eng 18(4):39-43
- Wu LZ, Selvadurai APS, Zhang LM, Huang RQ, Huang J (2016) Poro-mechanical coupling influences on potential for rainfall-induced shallow landslides in unsaturated soils. Adv Water Resour 98:114-121
- Yang KH, Uzuoka R, Lin GL, Nakai Y (2017) Coupled hydro-mechanical analysis of two unstable unsaturated slopes subject to rainfall infiltration. Eng Geol 216:13-30
- Yoo C, Jung HY (2006) Case history of geosynthetic reinforced segmental retaining wall failure. J Geotech Geoenviron 132(12):1538-1548
- Zhang LL, Zhang LM, Tang WH (2005) Rainfall-induced slope failure considering variability of soil properties. Geotechnique 55:183-188
- Zhao Y, Wang R, Jiang Y, Liu H, Wei Z (2019) GIS-based logistic regression for rainfallinduced landslide susceptibility mapping under different grid sizes in Yueging, southeastern China. Eng Geol 259:105147

Z. Song · L. Zhao

School of Civil Engineering, Central South University, Changsha, 410075, China

Z. Song

e-mail: songzhichen1219@gmail.com

L. Zhao

e-mail: zhaolianheng@csu.edu.cn

X. Li · J. J. Lizárraga · G. Buscarnera (🗷)

Department of Civil and Environmental Engineering, Northwestern University, Evanston, IL, USA Email: g-buscarnera@northwestern.edu

e-mail: xiangli2.2015@u.northwestern.edu